Compression and acceleration of ions by ultrashort, ultraintense azimuthally polarized light

Da-Chao Deng ⬤ and Hui-Chun Wu[*]

Institute for Fusion Theory and Simulation, School of Physics, Zhejiang University, Hangzhou 310058, China

An efficient plasma compression scheme using azimuthally polarized light is proposed. Azimuthally polarized light possesses a donutlike intensity pattern, enabling it to compress and accelerate ions toward the optical axis across a wide range of parameters. When the light intensity reaches the relativistic regime of 10^{18} W/cm^2, and the plasma density is below the critical density, protons can be compressed and accelerated by the toroidal soliton formed by the light. The expansion process of the soliton can be well described by the snowplow model. Three-dimensional particle-in-cell simulations show that within the soliton regime, despite the ion density exceeding ten times the critical density, the ions' energy is insufficient for efficient neutron production. When the light intensity increases to 10^{22} W/cm^2, and the plasma density reaches several tens of times the critical density, deuterium ions can be compressed to thousands of times the critical density and simultaneously accelerated to the MeV level by tightly focused azimuthally polarized light during the hole-boring process. This process is far more dramatic compared to the soliton regime and can produce up to 10^4 neutrons in a few light cycles. Moreover, in the subsequent beam-target stage, neutron yield is estimated to exceed 10^8. Finally, we present a comparison with the results obtained using a radially polarized light to examine the influence of light polarization.

I. INTRODUCTION

Neutron sources have broad applications in material testing for fusion energy research [1], neutron resonance spectroscopy [2], radiation medicine [3], etc. With the development of laser technology, laser-driven neutron sources are attracting great attention due to their compactness, high transportability, and ability for generating an ultrashort neutron pulse [4,5]. One of the currently investigated mechanisms capable of producing neutrons is nuclear-fusion reactions, suitable to being driven by laser owing to their relatively modest ion energy requirements compared to spallation reactions [4]. In the laser-driven schemes utilizing fusion reactions, ion acceleration is necessary to optimize neutron yields, as the reaction cross section peaks when the center-of-mass energy is on the order of keV to MeV, depending on the specific reaction involved [6]. There have been several laser-driven schemes based on different ion acceleration mechanisms, such as laser-cluster interactions by Coulomb explosion [7], in-target reactions by hole-boring mechanisms [8,9], and beam-target fusion by target normal sheath acceleration [8,10,11].

In order to enhance nuclear reactions within a limited time interval, some laser-driven schemes employ the ion compression at the same time of acceleration. Examples include spherically convergent plasma fusion [12–14], fusion enhanced by a double-cone configuration [15], and the collapse of a plasma shell using two ultraintense laser pulses [16]. In these schemes, ions can be compressed to 10 to 10^3 times the plasma critical density while being accelerated to MeV, aided by specific target configurations or multiple laser pulses.

Given that the reaction rate of nuclear fusion is proportional to the square of the ion density [6], compressing ions offers the potential to generate a substantial number of neutrons within a short period, thereby facilitating the production of a short neutron pulse. Furthermore, the ion compression via laser is a crucial concern for the exploit of inertial confinement fusion (ICF) energy. The current ion-compression schemes essentially possess structures similar to existing ICF schemes. There is a need for the exploration of novel plasma compression mechanisms, which can lead to new laser-driven schemes and also benefit ICF research.

In this paper, we propose an efficient ion compression mechanism, naturally achieved through the interaction of an ultrashort, ultraintense azimuthally polarized (AP) light with a uniform plasma, thereby eliminating the need for complex target configurations or multiple laser pulses. Recently, the focused laser intensity has exceeded 10^{23} W/cm^2 [17], and the generation of few-cycle cylindrical vector light over 10^{19} W/cm^2 has been achieved through pulse compression [18] or the use of an optical converter [19,20]. It is important to explore the phenomena induced by cylindrical vector light in the relativistic regime. Both AP and radially polarized (RP) lights are types of cylindrical vector light and share a cylindrically symmetric structure [21,22]. Their amplitude shape is the same as that of the Laguerre-Gaussian (LG) mode with the radial index $p = 0$ and the azimuthal index $l = 1$, denoted as the LG$_{01}$ mode [21]. Therefore, they typically exhibit a hollow intensity profile. When tightly focused, AP light generates a strong magnetic field along the optical axis on its focal point, whereas RP light gives a longitudinal electric field [23,24]. In the relativistic regime, an AP light is discovered to form a long-standing toroidal soliton when penetrating through an underdense plasma [25]. With a further increase in light

intensity and plasma density, the hole-boring process comes to dominate the laser-plasma interaction [26,27]. We will show that ions can be compressed and accelerated to different levels by an AP light in these relativistic-soliton and hole-boring regimes. It should be noted that the proposed plasma compression here does not work for a linearly [9,28,29] or circularly [30,31] polarized light with a simple Gaussian profile under the similar laser-plasma interaction condition.

The rest of the paper is organized as follows. In Sec. II we present the compression phenomenon in the soliton regime by 3D PIC simulation. An analytic theory based on the snowplow model is derived to describe the expansion of the toroidal soliton and plasma compression on its center. In Sec. III we investigate the compression and acceleration of deuterium ions in the hole-boring regime and estimate the neutron yields from the reaction $D + D \rightarrow {}^3He + n$. Additionally, a comparison with RP light is presented. Discussions and conclusions are given in Sec. IV.

II. THE SOLITON REGIME

A. PIC simulation setup

The PIC code used here is JPIC-3D [25,32,33], which adopts a field solver free of numerical dispersion along the x, y, z axes. AP light has an azimuthally directed electric field $\boldsymbol{E} = E_\theta \boldsymbol{e}_\theta$ in the cylindrical coordinates (r, θ, x), and E_θ can be expressed as [21]

$$E_\theta = \sqrt{2e}E_0 r \frac{w_0}{w(x)^2} \exp\left[-\frac{r^2}{w(x)^2}\right]$$
$$\times f(t) \exp\left\{i\left[kx - \omega t - 2\phi(x) + \frac{kr^2}{2R(x)}\right]\right\}, \quad (1)$$

where e denotes the natural number, $r = \sqrt{y^2 + z^2}$ is the transverse radius, $w(x) = w_0\sqrt{1 + x^2/X_R^2}$ is the beam width, $\phi(x) = \arctan(x/X_R)$ is the Gouy phase, $R(x) = x(1 + X_R^2/x^2)$ is the wavefront radius, $X_R = kw_0^2/2$ is the Rayleigh length, w_0 is the beam waist at the focal point and $k = 2\pi/\lambda$ is the wave number. The temporal profile takes $f(t) = \exp[-(t - x/c)^2/T_0^2]$, where T_0 is the pulse duration. The electric field amplitude E_0 can be normalized as $a_0 = eE_0/m_e\omega c$, where ω is the light angular frequency, m_e is electron mass, e is electron charge, and c is light speed. Laser intensity is given by $I_0[\text{W/cm}^2] \approx 1.37 \times 10^{18}\lambda_{\mu\text{m}}^{-2}a_0^2$.

In the soliton regime, the laser pulse takes $a_0 = 1$, which corresponds to $I \approx 1.37 \times 10^{18}$ W/cm^2 for the wavelength $\lambda = 1$ μm. The laser has the spot size $w_0 = 3$ and the duration $T_0 = 2$, i.e., 6.7 fs at $\lambda = 1$ μm. The laser pulse propagates from the left boundary at $x = 0$ and focuses on the plasma surface at $x = 1\lambda$. The plasma length is 6λ. The initial plasma density is $n_e = n_i = 0.7n_{cr}$, where $n_{cr} = \epsilon_0 m_e\omega^2/e^2$ is the plasma critical density, and ϵ_0 is the vacuum permittivity. The ions are chosen as protons with the mass $m_i = 1836m_e$. The initial temperatures are 10 eV for both electrons and ions.

The size of the simulation box is $8\lambda \times 10.67\lambda \times 10.67\lambda$, and the spatial resolution is 30 cells per wavelength, with each cell containing eight macroparticles. The time step is $30^{-1}\lambda/c$.
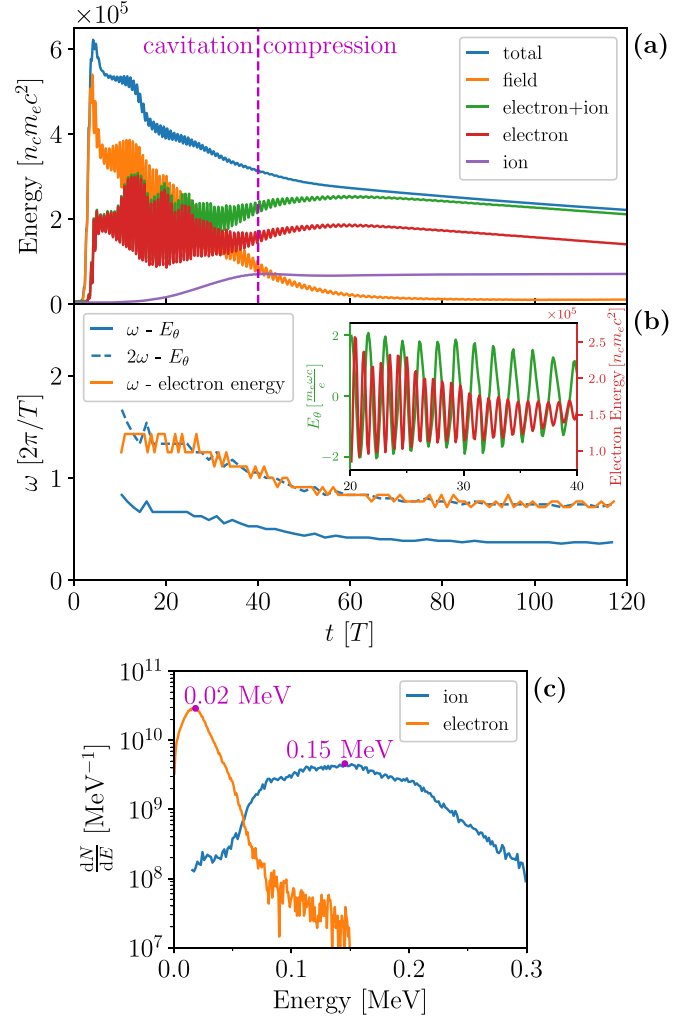

FIG. 1. (a) Temporal evolution of the field and particles energy in the simulation box. The magenta dashed line at $t = 40\lambda/c$ divides the cavitation and compression stages. (b) Oscillation frequency of the azimuthal electric field at $(x, y, z) = (4.3, 6.8, 5.3)\lambda$ and of the electron energy. The inset displays the temporal evolution of the azimuthal electric field and the electron energy from $t = 20\lambda/c$ to $40\lambda/c$. (c) Energy spectra of the electrons and ions in the red rectangular zone in Fig. 2(c).

B. Compression and acceleration process of the plasma

Figure 1(a) shows the energy evolution in the whole simulation box from $t = 0$ to $120\lambda/c$. The whole process consists of two stages: the cavitation stage before $t = 40\lambda/c$ and the compression stage thereafter. At the cavitation stage, the AP light has been fully input after $t = 6\lambda/c$. The electrons are accelerated rapidly with increasing kinetic energy by consuming laser field energy. A fraction of light is reflected out of the simulation box, which leads to the first steep descent of the total energy. The second steep descent occurring at $t \approx 16\lambda/c$ can be attributed to light transmission across the plasma out of the right boundary. Owing to the downshift in the light frequency below the background plasma frequency, a large part of light gets trapped in the plasma after $t = 20\lambda/c$. This trapped light then pushes electrons outward by the ponderomotive force, forming a subcycle toroidal soliton as first
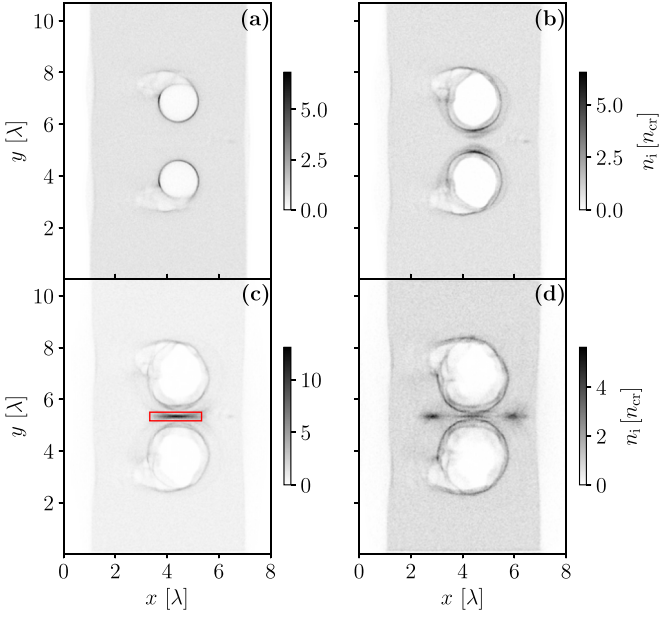
FIG. 2. Compression stage of the soliton. Ion density distributions taken in the x-y plane at $z = 5.3\lambda$ for $ct/\lambda = 40$ (a), 70 (b), 89.3 (c), 120 (d).

FIG. 3. (a) 3D diagram of the azimuthal electric field at $t = 40\lambda/c$. Projections in the x-y, y-z, and z-x planes show the electron density taken at $z = 5.3\lambda$, $x = 4.3\lambda$, and $y = 5.3\lambda$, respectively. The torus represents the plasma cavity, and the hollow cylinder is the approximation we use to model the enlargement of the annulus in the equatorial plane of the torus. r is the inner radius, R is the outer radius, and h is the thickness of the hollow cylinder. (b) Comparison of the results from the snowplow model and PIC simulation.

discussed in Ref. [25]. The decline of the total energy starts to exhibit a gentler slope since the trapped soliton slowly radiates out its energy. On a timescale of the ion response time $2\pi\omega_{\mathrm{pi}}^{-1}$, the ions initiate movement and cavitation in response to the space-charge field, marking the onset of the soliton's evolution into a postsoliton [25,28,34]. At $t = 40\lambda/c$, the ion energy climbs up to a flat form, and here an ion toroidal cavity forms as wide as the electron one as shown in Fig. 2(a).

After $t = 40\lambda/c$, as the ions gradually catch up the electrons, the whole toroidal plasma cavity enters into the compression stage. The toroidal postsoliton resembles a bent two-dimensional s-polarized postsoliton [34–36]. Therefore, ions on the inner side of the torus can be compressed and accelerated toward the torus center due to this distinct topological structure. Since the azimuthally directed electric field is tangential to the boundary of the toroidal cavity, the ponderomotive force exerted by the light on the plasma is more stable, resulting in a weak field-particle energy exchange. As a result, the amplitude of energy oscillations decreases in the compression stage, as shown in Fig. 1(a), and the subsequent compression is relatively moderate.

It should be noted that the ponderomotive force holds a crucial role in both the cavitation and compression stages. To see this, Fig. 1(b) shows that the oscillation frequency of the azimuthal electric field is exactly twice that of the electron energy (the inset shows temporally). This frequency characteristic arises from the fact that the pondermotive force of this azimuthal soliton contains a second harmonic oscillation [31] $f_p = -\frac{1}{4}m_e c^2 \nabla a^2 [1 + \cos(2\omega t)]$.

The later evolution of the compression stage is presented from Figs. 2(b) to 2(d). At $t = 70\lambda/c$, the particles on the inner side of the torus start to merge and penetrate with each other. At $t = 89.3\lambda/c$, they are compressed to a narrow density needle with a width of only around $0.6\lambda/c$. The
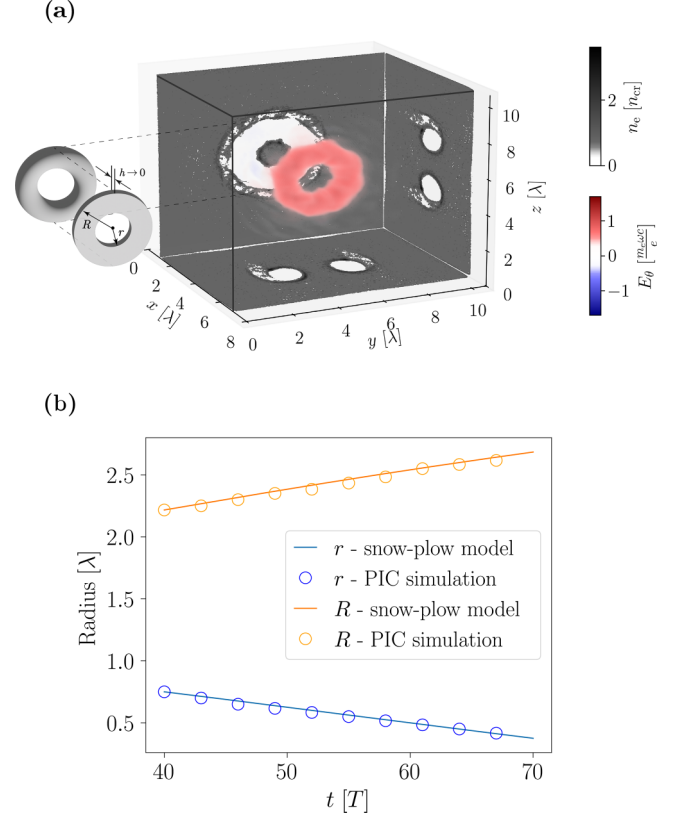
ion density reaches $n_i \simeq 13n_{\mathrm{cr}}$, ten times the initial density. Figure 1(c) gives the energy spectra of the particles in the red rectangular zone in Fig. 2(c). Fitted with the Maxwellian distribution, the ion spectrum reveals an effective ion temperature on the order of 0.1 MeV. This ion energy is relatively low for efficient neutron production [6]. By $t = 120\lambda/c$, the ion density needle has been further squeezed into two parts, traveling in opposite directions along the torus axis.

C. The snowplow model

The snowplow model has been used to study the long-term expansion of two-dimensional postsolitons formed by s-polarized lights in Refs. [34–36]. Here we employ the snowplow model to describe the expansion process of the toroidal cavity from $t = 40\lambda/c$ to $70\lambda/c$. First, as shown in Fig. 3(a), we use a flat hollow cylinder with an infinitesimal thickness h to approximately represent the enlargement of the annulus in the equatorial plane. Here r is its inner radius and R the outer radius. We use the subscripts "in" and "out" to distinguish the quantities on the inner and outer side of the torus. The snowplow model assumes that all the particles pushed by the light pressure $\simeq \epsilon_0 \langle E^2 \rangle /2$ are inside a thin shell. Let σ be
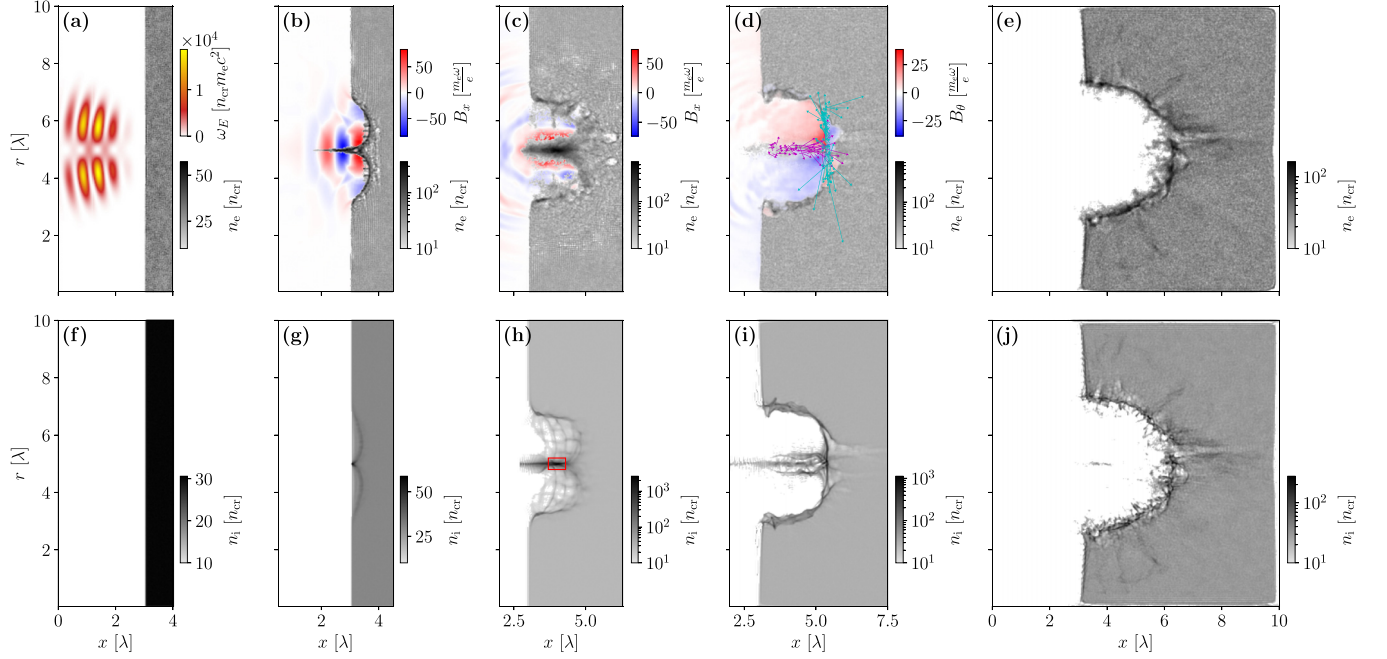
FIG. 4. Hole-boring compression process by the AP light. Electron density (a)–(e) and ion density (f)–(j) at $ct/\lambda = 4$ (a), (f), 6 (b), (g), 10.6 (c), (h), 16.8 (d), (i), and 40 (e), (j). The field energy density, longitudinal magnetic field, and azimuthal magnetic field are also shown in (a), (b) and (c), and (d), respectively. The magenta arrows in (d) represent the longitudinal current near the optical axis, and the cyan arrows represent the radial currents at the bottom of the plasma dip.

the ion surface number density in the cylindrical surface, and hence the plasma mass can be expressed as

$$M_{\text{in}} = 2\pi rhm_i\sigma_{\text{in}},$$
$$M_{\text{out}} = 2\pi Rhm_i\sigma_{\text{out}}, \qquad (2)$$

while noting that the electron mass has been neglected. By the particle number conservation, we have

$$2\pi rh\sigma_{\text{in}} = 2\pi r_0 h\sigma_{\text{in},0} + \pi(r_0^2 - r^2)hn_0,$$
$$2\pi Rh\sigma_{\text{out}} = 2\pi R_0 h\sigma_{\text{out},0} + \pi(R^2 - R_0^2)hn_0, \qquad (3)$$

where the subscript "0" denotes the initial quantities at $t = 40\lambda/c$. Here we further assume that the cylindrical surface with a radius of $(r_0 + R_0)/2$ is the interface between the inner and outer sides of the hollow cylinder. The total number of the ions on the inner side can then be calculated as

$$\begin{aligned} N_{\text{in}} = N\pi h &= 2\pi r_0 h\sigma_{\text{in},0} + \pi r_0^2 hn_0 \\ &= \pi R_0^2 hn_0 - 2\pi R_0 h\sigma_{\text{out},0} \\ &= \pi\left(\frac{R_0 + r_0}{2}\right)^2 hn_0, \end{aligned} \qquad (4)$$

where the term N, defined for convenience, is given as

$$N = n_0\left(\frac{R_0 + r_0}{2}\right)^2 \equiv n_0 L_0^2, \qquad (5)$$

where L_0 is the major radius of the torus. Substituting Eqs. (4) and (5) into Eq. (3), we obtain

$$\sigma_{\text{in}} = \frac{1}{2}\left(\frac{N}{r} - n_0 r\right), \quad \sigma_{\text{out}} = \frac{1}{2}\left(n_0 R - \frac{N}{R}\right). \qquad (6)$$

Since only the initial conditions and the particle number conservation law are used here, it can be seen that the surface number density, or plasma mass, is independent of the dynamical process in the snowplow model.

For the electric field, we can relate it to the cavity geometry by introducing the adiabatic invariant [34,37]

$$\int \frac{E^2}{\Omega}dV \qquad (7)$$

and by approximating the toroidal postsoliton as a resonant mode [38] $\Omega \sim \rho^{-1} = (R - r)^{-1}$. These two equations give

$$\langle E^2 \rangle \simeq \langle E_0^2 \rangle \left(\frac{R_0 - r_0}{R - r}\right)^3. \qquad (8)$$

Finally, the dynamical equations driven by the radiation pressure can be written as

$$\frac{d}{dt}\left(M_{\text{in}}\frac{dr}{dt}\right) = -2\pi rh\frac{\epsilon_0\langle E^2\rangle}{2},$$
$$\frac{d}{dt}\left(M_{\text{out}}\frac{dR}{dt}\right) = 2\pi Rh\frac{\epsilon_0\langle E^2\rangle}{2}, \qquad (9)$$

where M is the plasma mass. We then substitute Eqs. (2), (6), and (8) for Eqs. (9), and obtain the evolution equations of r and R as

$$(N - n_0 r^2)\frac{d^2 r}{dt^2} - 2n_0 r\left(\frac{dr}{dt}\right)^2 = -\frac{\epsilon_0 r}{m_i}\langle E_0^2\rangle\left(\frac{R_0 - r_0}{R - r}\right)^3,$$
$$(n_0 R^2 - N)\frac{d^2 R}{dt^2} + 2n_0 R\left(\frac{dR}{dt}\right)^2 = \frac{\epsilon_0 R}{m_i}\langle E_0^2\rangle\left(\frac{R_0 - r_0}{R - r}\right)^3. \qquad (10)$$

These equations are solved numerically, and Fig. 3(b) shows that the numerical solutions are in very good agreement with the PIC results.

III. THE HOLE-BORING REGIME

A. Azimuthally polarized light

In this section we attempt to enhance the plasma compression efficiency for a potential laser-driven neutron source by raising the light intensity and the initial plasma density. We will explore the so-called hole-boring regime in which AP light can directly compress and accelerate ions. The normalized light amplitude takes $a_0 = 150$, which corresponds to $I \approx 3.08 \times 10^{22}$ W/cm^2. The laser focus spot is shrunk to $w_0 = 1\lambda$, which can make the compression process faster and more efficient. When tightly focused to the wavelength scale, AP light can generate a longitudinal magnetic field as strong as the transverse field [23,24]. This field is helpful to confine the compressed electrons on the optical axis. In JPIC-3D, the laser-boundary-condition algorithm [39] is adopted to produce an ideal focus field [33]. The light is input at the left boundary and the focal plane is located at $x = 3\lambda$. The plasma has the initial density $n_0 = 30 n_{\mathrm{cr}}$. The ion mass is changed to $m_{\mathrm{i}} = 3672 m_{\mathrm{e}}$ to simulate a deuterium plasma. The size of the simulation box is $12\lambda \times 10\lambda \times 10\lambda$. All the other parameters remain the same as the soliton regime. Figure 4 illustrates the plasma compression process by the AP light. In Fig. 4(a) the tightly focused AP light exhibits a hollow intensity pattern, which punches out a ringlike dip on the plasma surface through the light pressure at $t = 6\lambda/c$, as shown in Figs. 4(b) and 4(g). The electrons on the optical axis are then squeezed backward and confined into a sharp needle by the ponderomotive force and the strong longitudinal magnetic field of the tightly focused AP light. The ions lag behind, following the movement of the electrons due to their space-charge field. Figure 5(a) illustrates the energy evolution of the system from $t = 0$ to $40\lambda/c$. At $t = 6\lambda/c$, discernible oscillations in both field and electron energies manifest the role of the ponderomotive force.

At $t = 10.6\lambda/c$, it is shown in Figs. 4(c) and 4(h) that the ions undergo compression, forming a ringlike dip comparable in width to that of the electrons and achieving the ion peak density of $n_{\mathrm{i}} \gtrsim 2600 n_{\mathrm{cr}}$ on the optical axis. This ion compression is mainly attributed to the electrostatic attraction exerted by the electrons compressed and confined on the optical axis. At this moment, as shown in Fig. 5(a), the energy oscillation tends to diminish, indicating that the light will soon be completely reflected from the plasma region. Figure 5(b) presents the energy spectra of the particles within the red rectangular zone in Fig. 4(h), revealing that the effective temperature of the ions reaches the order of 1 MeV, and that of the electrons is $\sim$10 MeV. The high density and energy of the ions are attained simultaneously, providing a suitable environment for producing neutrons in a short period through nuclear reactions. From the neutron yield formula [6] $Y = \frac{n_{\mathrm{D}}^2}{2} \langle \sigma_{\mathrm{D-D}} v \rangle V \Delta t$, where n_{D} is the deuterium density, $\langle \sigma_{\mathrm{D-D}} v \rangle$ is the average reactivity of the deuterium-deuterium reaction, V is the volume of the reaction region, and Δt is the reaction time, the neutron yield
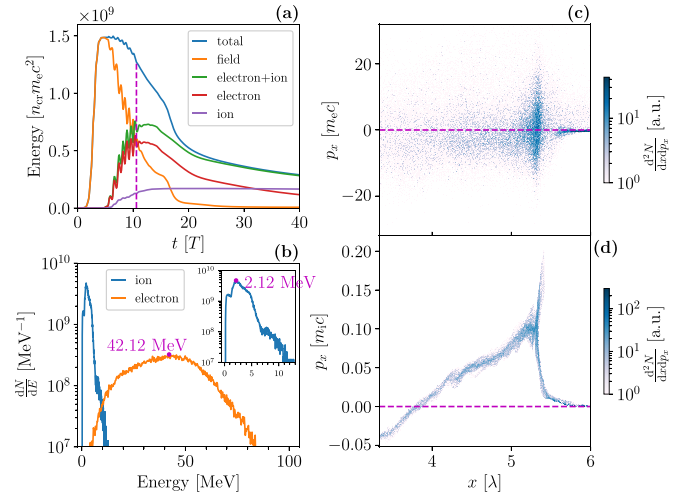

FIG. 5. Hole-boring dynamics by the AP light. (a) Temporal evolution of field and particle energy in the simulation box. The magenta dashed line marks $t = 10.6\lambda/c$. (b) Energy spectra of electrons and ions within the red rectangular zone in Fig. 4(h). (c), (d) Longitudinal momentum p_x vs position x for electrons and ions located in the zone covered by the magenta arrows in Fig. 4(d).

is estimated to be around 1.3×10^4 from $t = 8\lambda/c$ to $12\lambda/c$, spanning around 13 fs.

At $t = 16.8\lambda/c$ in Figs. 4(d) and 4(i), both compressed ions and electrons are further accelerated forward along the $+x$ direction and disperse slightly as the light departs, resulting in a decrease in the ion peak density to $n_{\mathrm{i}} \approx 1000 n_{\mathrm{cr}}$. The relatively high ion density is maintained by the strong azimuthal quasistatic magnetic field generated by the longitudinal current in the compressed plasma column. As presented in Figs. 5(c) and 5(d), the ions moving forward and a fraction of electrons moving backward dominate this positive longitudinal current. The presence of the radial currents is also observed at the bottom of the dip in Fig. 4(d). In Fig. 4(i) the fingerlike plasma channels are also discernible within the plasma due to the penetration of the light as a result of relativistically induced transparency [40].

Finally, the hole-boring process by the AP light leaves a U-shaped crater 3λ in depth and 2.4λ in diameter at $t = 40\lambda/c$ in Figs. 4(e) and 4(j). A significant portion of piled-up and accelerated ions would penetrate and travel through the deuterium plasma, giving rise to a substantial neutron yield via the beam-target approach. The neutron yield by this approach can be estimated using the integral [5,9,13]

$$Y = n_{\mathrm{D}} \int_0^\infty dE_{\mathrm{i}} f(E_{\mathrm{i}}) \int_0^{E_{\mathrm{i}}} dE \frac{\sigma(E)}{\varepsilon(E)}, \tag{11}$$

where $\sigma(E)$ is the reaction cross section and $\varepsilon(E)$ is the stopping power of the deuterium ion in the deuterium plasma. In our case the neutron yield resulting from the interaction of the injected deuterium ions and the deuterium plasma is approximately 1.16×10^8, much higher than the yield in the compression stage owing to a sufficient reaction time.
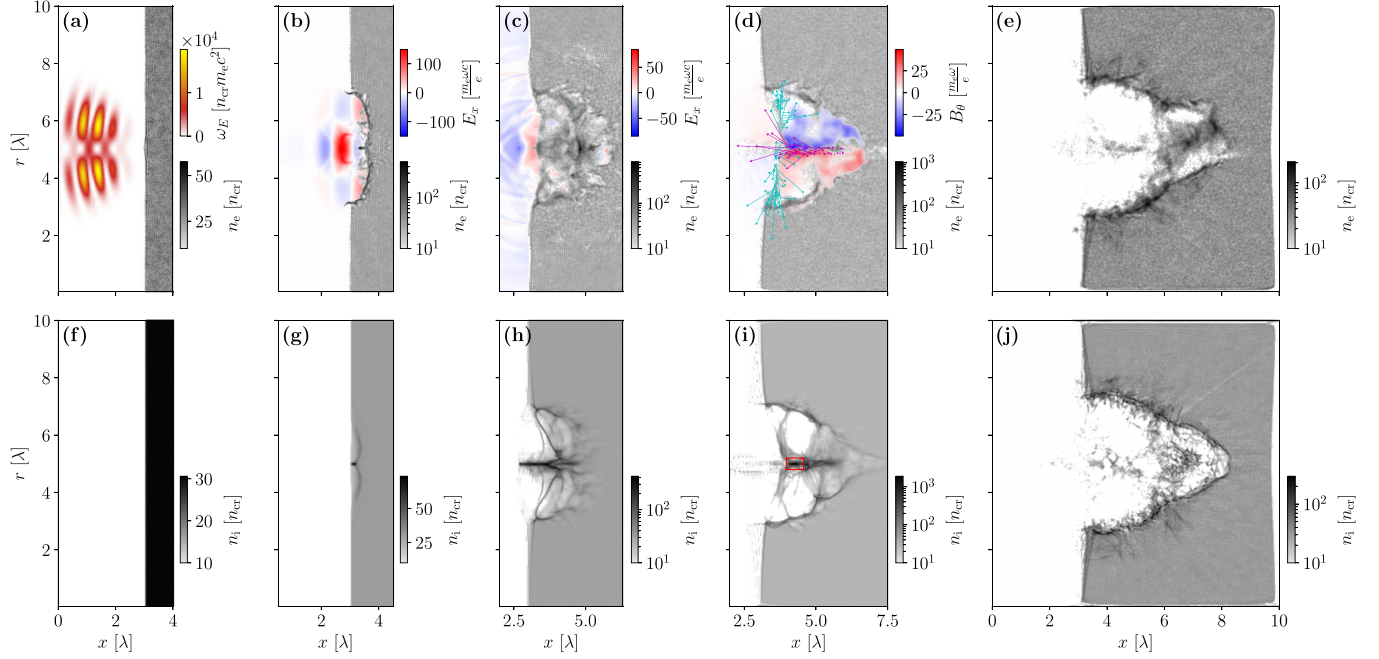
FIG. 6. Hole-boring compression process by the RP light. Same as Fig. 4 with two exceptions: first, it is longitudinal electric fields, rather than magnetic fields, which are shown in (b) and (c); second, radial currents are located at the top, rather than bottom, of the plasma dip in (d).

B. Radially polarized light

AP light has been shown to be a robust natural mode for forming a long-standing toroidal soliton with a relatively moderate plasma compression. In fact, the change in polarization can influence its geometry and stability [41]. However, the hole-boring regime discussed above seems to be mainly dominated by the light ponderomotive force, which is simply proportional to the gradient of intensity distribution [42]. To check the potential polarization effects in the hole-boring regime, a case using RP light is displayed in Figs. 6 and 7, with the other parameters fixed. The expression for RP light can be directly derived from that for AP light through the duality transformation [43] $E \rightarrow cB$ and $B \rightarrow -E/c$. Thus, both lights share the same intensity pattern [24] as can be verified by comparing Figs. 4(a) and 6(a). Due to the exchange of the electric and magnetic field alignments for both types of light, a strong longitudinal electric field, rather than a magnetic field, appears when RP light is tightly focused.

The polarization change has an impact on the compression and acceleration of ions. Figure 7(a) presents the temporal evolution of the maximum ion density near the optical axis for both polarization states. Two observations can be made: first, the ion peak density achieved by RP light is 28% lower than that in the AP case; second, the time $t = 16.8\lambda/c$ at which the ion density peaks for RP light is delayed compared to that for AP light. In fact, as shown in Fig. 7(b), there is no oscillation in the field or electron energy at $t = 16.8\lambda/c$, which means that the light has been completely scattered away from the plasma region.

To explain the difference in the results, we shall examine the compression process more closely. As shown in Fig. 6(b), the electrons on the optical axis are pushed into the plasma
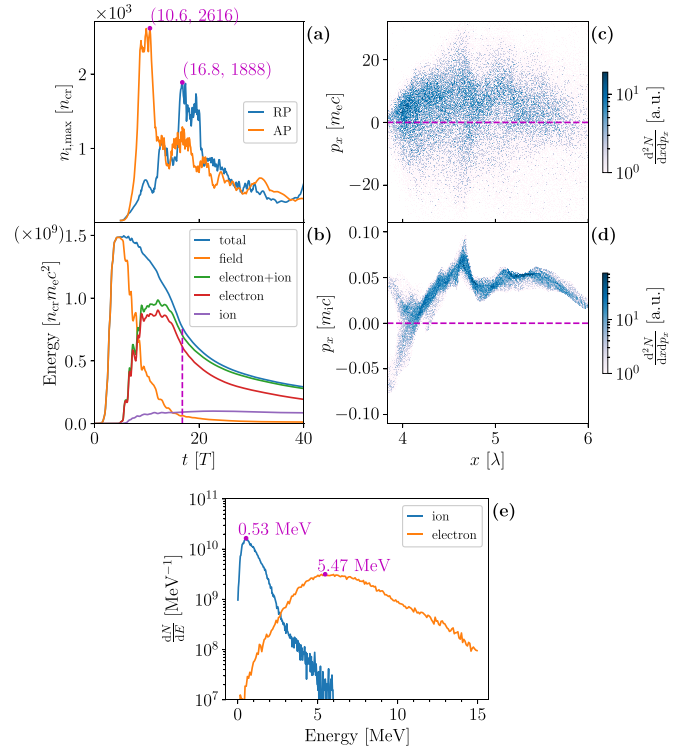

FIG. 7. Hole-boring dynamics by the RP light. (a) Temporal evolution of the maximum ion density achieved by AP or RP light near the optical axis. (b) Temporal evolution of field and particle energy in the simulation box. The magenta dashed line marks $t = 16.8\lambda/c$. (c), (d) p_x vs x for particles located in the zone covered by the magenta arrows in Fig. 6(d). (e) Energy spectra of electrons and ions within the red rectangular zone in Fig. 6(i).

rather than squeezed out in Fig. 4(b). The ion motion, which reflects the hollow structure of RP light, is illustrated in Fig. 6(g). As the light penetrates deeper, the electrons are pulled back by the reversed longitudinal electric field in the second subcycle. This push-pull action [44] shakes the electrons longitudinally, along with radially oscillating motion induced by the radial electric field in the interaction region. As a result, the electrons cannot be stably confined on the optical axis, leading to a lower ion density.

When the light leaves off the plasma region at $t = 16.8\lambda/c$, as shown in Figs. 6(d) and 6(i), a negative longitudinal current is formed, generating a strong quasistatic azimuthal magnetic field. As seen in Figs. 7(c) and 7(d), the majority of electrons accelerated by its longitudinal electric field possess a positive longitudinal momentum, leading to this negative longitudinal current. This resulting azimuthal magnetic field pinches the electron current into a filament [45], subsequently drawing the ions toward the axis, analogous to the Z-pinch process [46,47]. In addition, the radial current induced by the electrons moving from the radial boundary of the plasma to the optical axis can be found at the top of the dip, as shown in Fig. 7(d), resulting in the reversed azimuthal magnetic field on both sides.

The energy spectra of the particles within the red rectangular zone in Fig. 6(i), when the ion density reaches its peak, are presented in Fig. 7(e). The effective ion and electron temperatures are only about 0.1 MeV and 1 MeV, respectively, both nearly one order of magnitude lower than that of the AP case. This is mainly because most of the energetic electrons accelerated by the push-pull mechanism [44] have exited the compression region as the light departs, resulting in low energy transfer to the ions.

The neutron yield from nuclear reactions between $t = 15.8\lambda/c$ and $19.8\lambda/c$ is estimated to be 9.3×10^3, and the subsequent beam-target yield is estimated to be 2.38×10^7. Both are lower than in the AP case. Nevertheless, due to the strong longitudinal electric field of the RP light, the crater in Figs. 6(e) and 6(j) exhibits a width of 1.3 λ and a significantly greater depth of 5.5 λ compared to that created by the AP light.

IV. DISCUSSION AND CONCLUSION

In the hole-boring regime, a wide parameter range is scanned by changing light intensity and initial density. We find that to achieve optimum ion compression with the highest density, a proportionate balance between light intensity and plasma density should be maintained. If the plasma is too dense or the light is too weak, AP light is not able to drill deep enough to compress ions. Conversely, if the plasma is too rarefied or the light is too strong, the number of the ions involved in the compression is not large enough compared to that the light could compress.

Interestingly, it is noteworthy that even within the hole-boring regime, AP light can be trapped in the ringlike plasma dip for several light cycles, behaving like a short-term soliton, as shown in Figs. 8(a) and 8(b). This case takes a relatively low light amplitude $a_0 = 50$ for a plasma density $n_0 = 10n_{\text{cr}}$. Compared to the case in Fig. 2, the shorter duration of the toridal soliton is because the compression is much faster due to a smaller focal spot and a higher light intensity. It is hard to
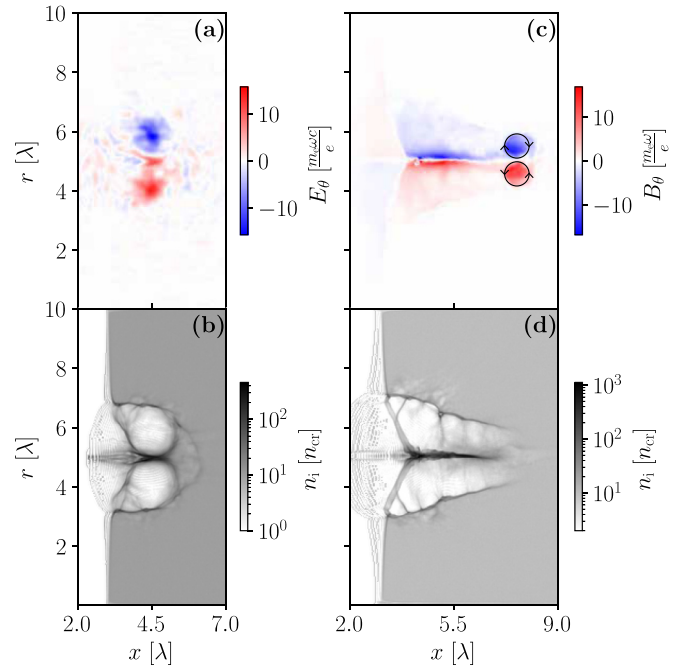

FIG. 8. Intermediate case for $a_0 = 50$ and $n_0 = 10n_{\text{cr}}$, and all other parameters are the same as Fig. 4. AP light: azimuthal electric field (a) and ion density (b) at $t = 18.8\lambda/c$. RP light: azimuthal magnetic field (c) and ion density (d) at $t = 25.9\lambda/c$. The black arrows in (c) point the direction of the electric currents.

distinguish between the soliton and hole-boring stage clearly within such a set of intermediate parameters. The case using RP light is also shown in Figs. 8(b) and 8(d). The peak densities of deuterium ions reach $n_i \approx 500n_{\text{cr}}$ and $1000n_{\text{cr}}$ for AP and RP lights, respectively. Additionally, Fig. 8(c) illustrates that vortex electric currents can be generated, giving rise to a robust quasistatic azimuthal magnetic field. This toroidal vortex is similar to that observed by using a Gaussian-shape light [48]. The RP light in this case can finally penetrate through the plasma and release its energy at the plasma-vacuum interface in the right. Annihilation of the vortex magnetic field can produce the electric field [49], which has the potential to efficiently accelerate the ions through the Magnetic Vortex Acceleration mechanism [50–53].

In terms of the polarization effect, we primarily focus on these two cylindrical vector lights, as they have a cylindrically symmetric structure, ensuring a more uniform and stable compression and acceleration of ions and facilitating the analysis in both theory and simulation. On the other hand, LG$_{01}$ light of linear or circular polarization has also demonstrated the potential to form a toroidal ion cavity in plasma [54,55] or compress ions toward the optical axis [56]. However, to the best of our knowledge, there has been no detailed discussion of the ion compression effect by ultrashort LG$_{01}$ lights of these polarizations in the soliton or hole-boring regime. Since these polarization states can be considered as a linear superposition of azimuthal and radial components in the cylindrical polarization bases [57,58], our investigation of these two fundamental cylindrical vector lights can serve as a foundation for further research concerned with polarization or other degrees of freedom in light, such as angular momentum [58].

In conclusion, our 3D PIC simulations show that the ion compression and acceleration can be realized efficiently by an AP light across a wide range of parameters. In the soliton regime, an AP light with an intensity of 10^{18} W/cm^2 can form a toroidal soliton and compress ions from $0.7n_{cr}$ to $13n_{cr}$, over ten times the initial density. However, the ion energy is only on the 0.1 MeV level, insufficient for efficient neutron production. Based on the snowplow model and some approximations, an analytic theory is derived to demonstrate the expansion of the toroidal cavity. In the hole-boring regime, an AP light with an intensity of 10^{22} W/cm^2 is adopted to drill into a deuterium plasma with an initial density of $n_0 = 30n_{cr}$. The peak deuterium ion density can exceed $2600n_{cr}$, nearly 100 times the initial density, and the ion energy can attain the MeV level. This efficient compression and acceleration of ions is appropriate for nuclear fusions. Here we consider the deuterium-deuterium reaction to estimate the neutron yields in different stages. In the compression stage, the neutron yield is 1.3×10^4 in 13 fs. The compressed ions can subsequently trigger nuclear fusions by the beam-target reactions as they penetrate through the deuterium plasma. In this stage, the neutron yield is around 10^8, much higher than the yield in the compression stage due to the sufficient reaction time. To highlight the light polarization effect, ion compression by RP light is also examined. The dominant compression process by RP light resembles a Z pinch.

[1] L. J. Perkins, B. G. Logan, M. D. Rosen, M. D. Perry, T. D. de la Rubia, N. M. Ghoniem, T. Ditmire, P. T. Springer, and S. C. Wilks, Nucl. Fusion **40**, 1 (2000).

[2] D. P. Higginson, J. M. McNaney, D. C. Swift, T. Bartal, D. S. Hey, R. Kodama, S. Le Pape, A. Mackinnon, D. Mariscal, H. Nakamura *et al.*, Phys. Plasmas **17**, 100701 (2010).

[3] D. Schardt, T. Elsässer, and D. Schulz-Ertner, Rev. Mod. Phys. **82**, 383 (2010).

[4] A. Alejo, H. Ahmed, A. Green, S. R. Mirfayzi, M. Borghesi, and S. Kar, Nuovo Cimento C **38C**, 1 (2016).

[5] A. Yogo, Y. Arikawa, Y. Abe, S. R. Mirfayzi, T. Hayakawa, K. Mima, and R. Kodama, Eur. Phys. J. A **59**, 191 (2023).

[6] S. Atzeni and J. Meyer-ter-Vehn, *The Physics of Inertial Fusion: Beam Plasma Interaction, Hydrodynamics, Hot Dense Matter*, International Series of Monographs on Physics (Clarendon Press, Oxford, 2004), Vol. 125.

[7] T. Ditmire, J. Zweiback, V. P. Yanovsky, T. E. Cowan, G. Hays, and K. B. Wharton, Nature (London) **398**, 489 (1999).

[8] L. Willingale, G. M. Petrov, A. Maksimchuk, J. Davis, R. R. Freeman, A. S. Joglekar, T. Matsuoka, C. D. Murphy, V. M. Ovchinnikov, A. G. R. Thomas *et al.*, Phys. Plasmas **18**, 083106 (2011).

[9] C. Toupin, E. Lefebvre, and G. Bonnaud, Phys. Plasmas **8**, 1011 (2001).

[10] X. Jiang, F. Shao, D. Zou, M. Yu, L. Hu, X. Guo, T. Huang, H. Zhang, S. Wu, G. Zhang *et al.*, Nucl. Fusion **60**, 076019 (2020).

[11] J. Yan, G. L. Ren, Z. J. Chen, X. Zhang, C. Yang, L. L. Li, J. H. Zheng, H. Cao, C. K. Sun, W. Jiang *et al.*, Nucl. Fusion **62**, 106030 (2022).

[12] H. B. Zhuo, W. Yu, M. Y. Yu, H. Xu, X. Wang, B. F. Shen, Z. M. Sheng, and J. Zhang, Phys. Rev. E **79**, 015401(R) (2009).

[13] M.-Q. He, H.-B. Cai, H. Zhang, Q.-L. Dong, C.-T. Zhou, S.-Z. Wu, Z.-M. Sheng, L.-H. Cao, C.-Y. Zheng, J.-F. Wu *et al.*, Phys. Plasmas **22**, 123103 (2015).

[14] G. Ren, J. Yan, J. Liu, K. Lan, Y. H. Chen, W. Y. Huo, Z. Fan, X. Zhang, J. Zheng, Z. Chen *et al.*, Phys. Rev. Lett. **118**, 165001 (2017).

[15] L.-X. Hu, T.-P. Yu, F.-Q. Shao, Q.-J. Zhu, Y. Yin, and Y.-Y. Ma, Phys. Plasmas **22**, 123104 (2015).

[16] H. Xu, W. Yu, M. Y. Yu, A. Y. Wong, Z. M. Sheng, M. Murakami, and J. Zhang, Appl. Phys. Lett. **100**, 144101 (2012).

[17] J. W. Yoon, Y. G. Kim, I. W. Choi, J. H. Sung, H. W. Lee, S. K. Lee, and C. H. Nam, Optica **8**, 630 (2021).

[18] F. Kong, H. Larocque, E. Karimi, P. B. Corkum, and C. Zhang, Optica **6**, 160 (2019).

[19] S. Carbajo, E. Granados, D. Schimpf, A. Sell, K.-H. Hong, J. Moses, and F. X. Kärtner, Opt. Lett. **39**, 2487 (2014).

[20] S. Carbajo, E. A. Nanni, L. J. Wong, G. Moriena, P. D. Keathley, G. Laurent, R. J. Dwayne Miller, and F. X. Kärtner, Phys. Rev. Accel. Beams **19**, 021303 (2016).

[21] Q. Zhan, Adv. Optics Photonics **1**, 1 (2009).

[22] A. Forbes, Laser Photonics Rev. **13**, 1900140 (2019).

[23] S. Quabis, R. Dorn, M. Eberler, O. Glöckl, and G. Leuchs, Opt. Commun. **179**, 1 (2000).

[24] R. Dorn, S. Quabis, and G. Leuchs, Phys. Rev. Lett. **91**, 233901 (2003).

[25] Z. Cheng, D. Deng, M. Yu, and H. Wu, Plasma Sci. Tech. **25**, 032001 (2023).

[26] C. Yu, A. Deng, Y. Tian, W. Li, W. Wang, Z. Zhang, R. Qi, C. Wang, and J. Liu, Phys. Plasmas **23**, 082701 (2016).

[27] J. Psikal and M. Matys, Plasma Phys. Control. Fusion **60**, 044003 (2018).

[28] T. Esirkepov, K. Nishihara, S. V. Bulanov, and F. Pegoraro, Phys. Rev. Lett. **89**, 275002 (2002).

[29] G. Sarri, D. K. Singh, J. R. Davies, F. Fiuza, K. L. Lancaster, E. L. Clark, S. Hassan, J. Jiang, N. Kageiwa, N. Lopes *et al.*, Phys. Rev. Lett. **105**, 175007 (2010).

[30] Z. Li, Y. Bai, and Y. Tian, Opt. Lett. **46**, 336 (2021).

[31] S. M. Weng, M. Murakami, P. Mulser, and Z. M. Sheng, New J. Phys. **14**, 063026 (2012).

[32] H.-C. Wu, arXiv:1104.3163.

[33] Z.-M. Cheng, H.-C. Wu, D.-C. Deng, and M.-Y. Yu, Phys. Plasmas **30**, 073105 (2023).

[34] N. M. Naumova, S. V. Bulanov, T. Zh. Esirkepov, D. Farina, K. Nishihara, F. Pegoraro, H. Ruhl, and A. S. Sakharov, Phys. Rev. Lett. **87**, 185004 (2001).

[35] G. Sánchez-Arriaga and E. Lefebvre, Phys. Rev. E **84**, 036403 (2011).

[36] G. Sánchez-Arriaga and E. Lefebvre, Phys. Rev. E **84**, 036404 (2011).

[37] L. D. Landau and E. M. Lifshits, *Electrodynamics of Continuous Media*, 2nd ed., Course of Theoretical Physics (Pergamon Press, Oxford, 1984), Vol. 8.

[38] F. Cap and R. Deutsch, IEEE Trans. Microwave Theory Tech. **26**, 478 (1978).

[39] I. Thiele, S. Skupin, and R. Nuter, J. Comput. Phys. **321**, 1110 (2016).

[40] A. Pukhov and J. Meyer-ter-Vehn, Phys. Rev. Lett. **79**, 2686 (1997).

[41] Z. Li, S. Guo, Y. Bai, Y. Zeng, and Y. Tian, Plasma Phys. Control. Fusion **63**, 015007 (2021).

[42] G. A. Mourou, T. Tajima, and S. V. Bulanov, Rev. Mod. Phys. **78**, 309 (2006).

[43] A. April, Ultrashort, strongly focused laser pulses in free space, in *Coherence and Ultrashort Pulse Laser Emission*, edited by F. J. Duarte (InTech, Rijeka, Croatia, 2010), pp. 355–382.

[44] N. Zaïm, M. Thévenet, A. Lifschitz, and J. Faure, Phys. Rev. Lett. **119**, 094801 (2017).

[45] N. M. Naumova, J. Koga, K. Nakajima, T. Tajima, T. Zh. Esirkepov, S. V. Bulanov, and F. Pegoraro, Phys. Plasmas **8**, 4149 (2001).

[46] S. A. Slutz, M. C. Herrmann, R. A. Vesey, A. B. Sefkow, D. B. Sinars, D. C. Rovang, K. J. Peterson, and M. E. Cuneo, Phys. Plasmas **17**, 056303 (2010).

[47] O. A. Hurricane, P. K. Patel, R. Betti, D. H. Froula, S. P. Regan, S. A. Slutz, M. R. Gomez, and M. A. Sweeney, Rev. Mod. Phys. **95**, 025005 (2023).

[48] D. N. Yue, M. Chen, P. F. Geng, X. H. Yuan, Z. M. Sheng, J. Zhang, Q. L. Dong, A. Das, and G. R. Kumar, Plasma Phys. Contol. Fusion **63**, 075009 (2021).

[49] K. V. Lezhnin, F. F. Kamenets, T. Zh. Esirkepov, and S. V. Bulanov, J. Plasma Phys. **84**, 905840610 (2018).

[50] S. V. Bulanov and T. Zh. Esirkepov, Phys. Rev. Lett. **98**, 049503 (2007).

[51] T. Nakamura, S. V. Bulanov, T. Z. Esirkepov, and M. Kando, Phys. Rev. Lett. **105**, 135002 (2010).

[52] M. H. Helle, D. F. Gordon, D. Kaganovich, Y. Chen, J. P. Palastro, and A. Ting, Phys. Rev. Lett. **117**, 165001 (2016).

[53] J. Park, S. S. Bulanov, J. Bin, Q. Ji, S. Steinke, J.-L. Vay, C. G. R. Geddes, C. B. Schroeder, W. P. Leemans, T. Schenkel, and E. Esarey, Phys. Plasmas **26**, 103108 (2019).

[54] T. C. Wilson, F. Y. Li, S. M. Weng, M. Chen, P. McKenna, and Z. M. Sheng, J. Phys. B: At. Mol. Opt. Phys. **52**, 055403 (2019).

[55] T. C. Wilson, Z.-M. Sheng, P. McKenna, and B. Hidding, J. Phys. Commun. **7**, 035002 (2023).

[56] W. Wang, B. Shen, X. Zhang, L. Zhang, Y. Shi, and Z. Xu, Sci. Rep. **5**, 8274 (2015).

[57] J. J. Gil and R. Ossikovski, *Polarized Light and the Mueller Matrix Approach* (CRC Press, Boca Raton, FL, 2016).

[58] Q. Zhan, Opt. Lett. **31**, 867 (2006).